SUPPLEMENTARY MATERIAL

A: Continuous phase flow analysis using Particle Image Velocimetry (PIV)

The continuous phase flow is analyzed by Particle Image Velocimetry (PIV) (without dispersed phase injection) in order to find the unperturbed continuous phase velocity v_{cp} at the location of the bound drop center of mass. To do so, a 5 µm-Polyamid Seeding Particles solution (with a small amount of surfactant to disperse the particles) is pumped through the cell, with 50 images analyzed per flow rate (DynamicStudio, Dantec Dynamics), at least in triplicate. The camera, lens and light source are those of Section II. We use a resolution of 1280 × 400 px² and an acquisition frequency of 6559 Hz. Adaptive PIV is performed with a final grid step size of 16 × 16 px².

We investigate the different continuous phase volumetric flow rates q_{cp} tested in the present work. For each q_{cp}, we obtain an average velocity vector map (Fig. A1). The continuous phase velocity v_{cp} seen by a growing drop is determined from the map by the following method. We report the velocity component along the x-axis as a function of the position above the capillary y (Fig. A2). We note that this is done for a position x corresponding to the centre of the nozzle. We see that the continuous phase velocity above the nozzle is essentially uniform, except for in a thin adjacent layer, corresponding to the boundary-layer. As mentioned in Section II, in our case, drops are mainly located above this layer. As a result, we consider that the continuous phase velocity v_{cp} seen by a growing drop corresponds to the velocity measured in the uniform flow above the shear layer. Therefore, in the example of Fig. A2, we consider that $v_{cp} = 0.57$ m.s^{-1}.

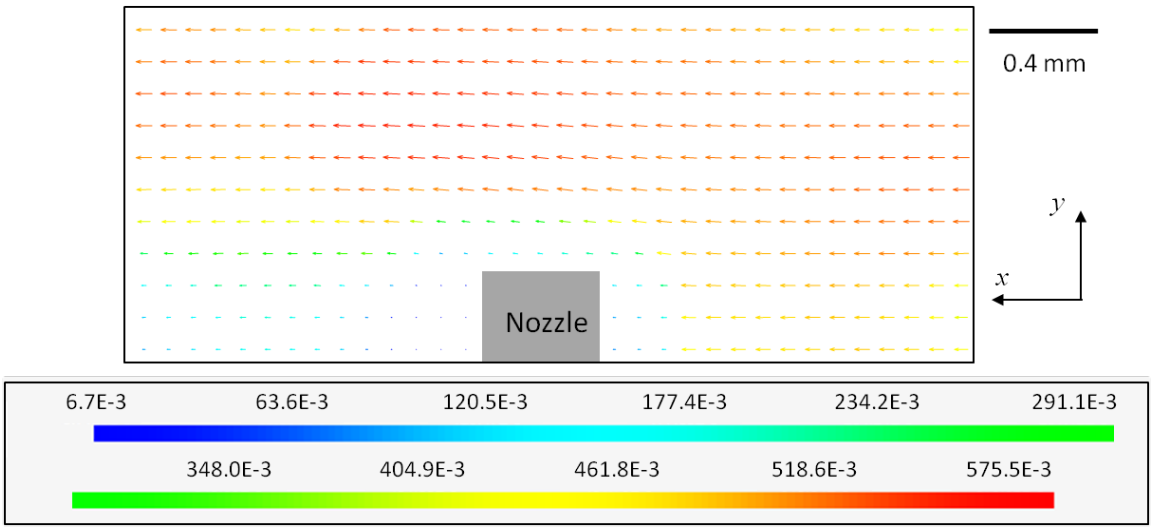

FIG. A1: Average velocity vector map in the centre of the cell channel at a continuous phase flow rate of 45.3 L.h^{-1}. Velocity scale below in m.s^{-1}; nozzle tip superimposed in grey.

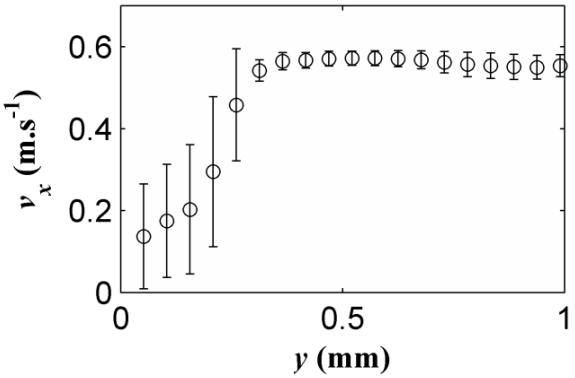

FIG. A2: Velocity component along the x-axis function of the position above the capillary y, for the example of Fig. A1.

B: Oscillations in jet widening

In Fig. B1, we show a chronological sequence of snapshots for a jet formed in the widening regime, for the reference system. From this, we can see the complex behavior of the thread, with surface oscillations which occur. These oscillations seem stationary in space. According to Utada *et al.*[20] who studied jet widening in coflowing liquids, this behavior is characteristic of an absolute instability.

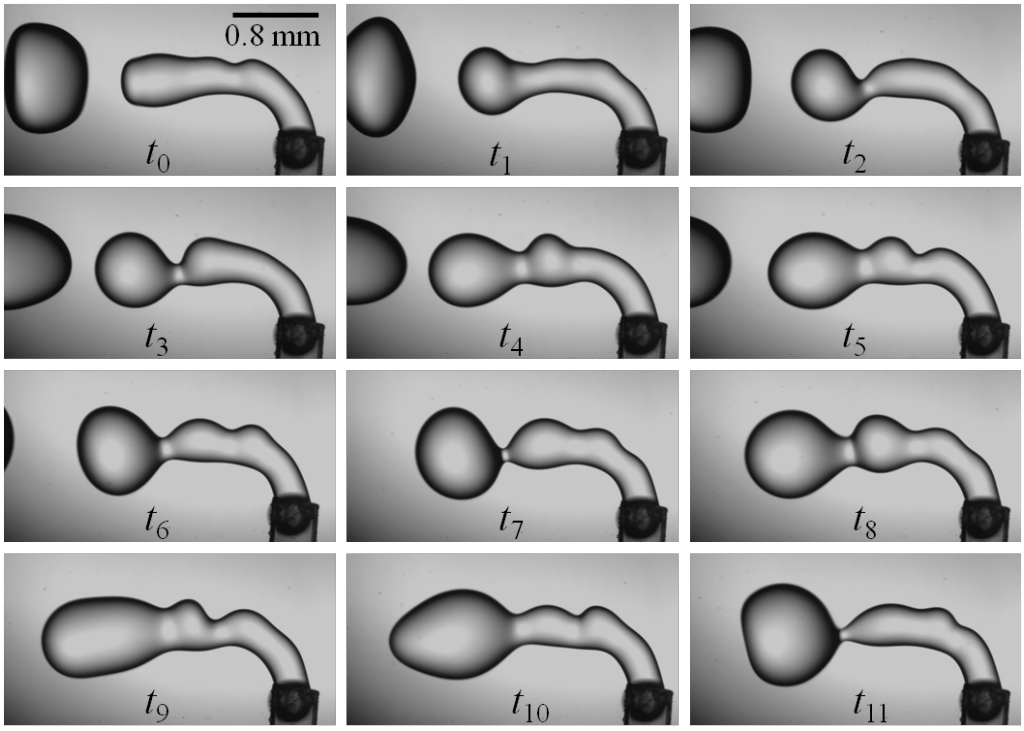

FIG. B1: Illustration of thread surface oscillations in jet widening: snapshots for the reference system ($\mathrm{Oh}_{cp} = 7.0\times10^{-3}$), $\mathrm{We}_{\mathrm{in}} = 2.04$, $\mathrm{Ca}_{\mathrm{out}} = 5.1\times10^{-3}$. t_0 is the initial point, taken just after the previous drop detachment, $t_n = t_{n-1} + 656\ \mu s$ and finally, the current drop detaches between t_{11} and t_{12}.

As Utada *et al.*[20], we further quantified these oscillations by focusing on the drop neck (between the drop and the thread). We measured the drop neck diameter variations in time (Fig. B2). It can be seen that the neck diameter oscillates about its mean with an increasing amplitude until pinch-off, followed by drop detachment. The oscillation amplitude grows more rapidly for the reference system (black points, Fig. B2) than for system 1 (grey points, Fig. B2).

From various curves such as in Fig. B2, we estimate the neck oscillation frequency f_c for the reference system (350 Hz), system 1 (164 Hz) and system 2 (72 Hz). This gives characteristic growth times $\tau_c = 1/f_c$. We find that the necking time τ_n as calculated in Section IV.B is in the order of τ_c. τ_n is 1.4 to 2.5 times higher than τ_c, depending on the system.

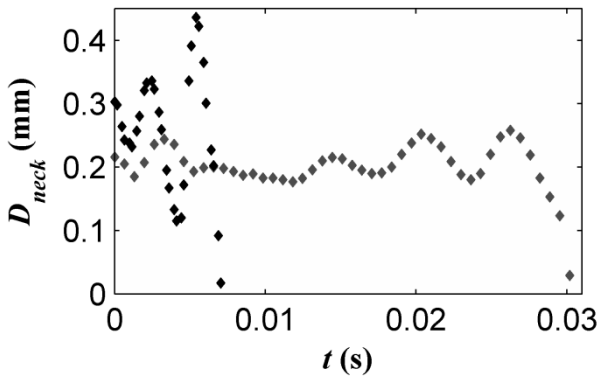

FIG. B2: Drop neck diameter variations in time for: reference system, $\mathrm{We}_{\mathrm{in}} = 2.04$ and $\mathrm{Ca}_{\mathrm{out}} = 5.1\times10^{-3}$ (black); system 1, $\mathrm{We}_{\mathrm{in}} = 0.82$ and $\mathrm{Ca}_{\mathrm{out}} = 6.8\times10^{-3}$ (grey).

C: Collapsed data in jet narrowing

In Section IV.A, we noted that the transition from jet widening to narrowing is shifted towards higher $\mathrm{Ca_{out}}$ values as the interfacial tension decreases. This trend was not reported before. However, in our trials, the drag force experienced by a growing drop corresponds to that for an inertial flow since the particle Reynolds number $\mathrm{Re_p}$ ranges from 114 to 424. This is far from the $\mathrm{Re_p}$ range of Pathak's[22] cross-flow simulations, Meyer and Crocker's[21] cross-flow experiments or Utada *et al.*'s[20] coflow experiments. Indeed, $\mathrm{Re_p}$ ranges from about 10 to 50 in Pathak's simulations, from 2 to 150 in Meyer and Crocker's trials and from 2 to 10 in Utada *et al.*'s experiments. These $\mathrm{Re_p}$ ranges are much closer to creeping flow than ours.

Under Newton regime assumption, the ratio of the drag force to the capillary force is in order of $(\mathrm{Ca_{out}}/\mathrm{Oh}_{cp})^2 = \mathrm{We_{out}}$ (as opposed to $\mathrm{Ca_{out}}$ under Stokes approximation). We therefore propose to plot the critical inner Weber number $\mathrm{We_{in}}$ as a function of $\mathrm{Ca_{out}}/\mathrm{Oh}_{cp}$ (Fig. C1): it appears that our data in fact collapse in the narrowing regime.

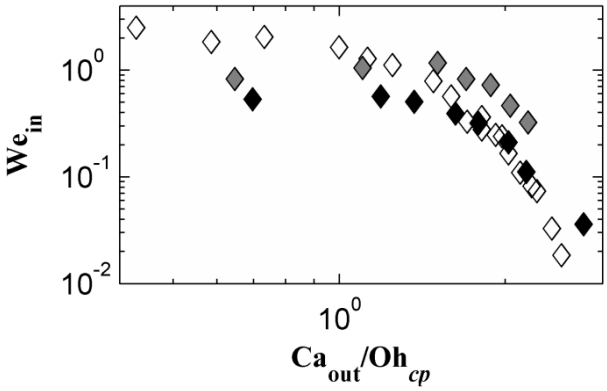

FIG. C1: $\mathrm{We_{in}}$ function of $\mathrm{Ca_{out}}/\mathrm{Oh}_{cp}$, see Table I for symbols.

D: Comparison with Pathak's and Meyer and Crocker's DJT criteria

Fig. D1 presents the DJT data obtained for the reference system in the $\mathrm{Ca_{out}}-\mathrm{We_{in}}$ space, together with Pathak's[22] and Meyer and Crocker's[21] DJT criteria. The outer capillary number in Pathak's criterion is originally built with the mean continuous phase velocity (ratio of the volumetric flow rate to the channel section for the continuous phase flow). To calculate Pathak's criterion, we presently assimilate the mean continuous phase velocity to v_{cp}, the velocity effectively seen by a growing drop. The outer capillary number in Meyer and Crocker's criterion is built with the continuous phase wall shear rate and the nozzle inner diameter. To calculate Meyer and Crocker's criterion, we consider that the continuous phase velocity at the distance D_p from the nozzle tip is close to v_{cp}.

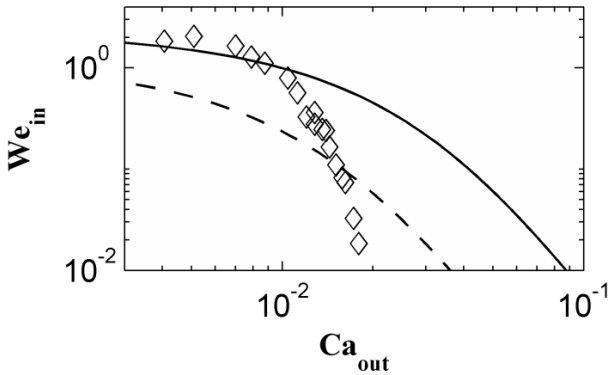

FIG. D1: $\mathrm{We_{in}}$ function of $\mathrm{Ca_{out}}$ at the DJT, see Table I for symbols. Pathak's DJT criterion (dashed line); Meyer and Crocker's DJT criterion (solid line).

Fig. D1 shows that the reference system data are not satisfactorily described by Pathak's criterion (dashed line), nor by Meyer and Crocker's criterion (solid line). Two main reasons may be advanced:

(i) in our trials, the growing drop is mainly located above the shear layer adjacent to the nozzle tip whereas in the previous authors' work, the drop is entirely located in the shear layer; (ii) the hydrodynamic regime of the drag force experienced by the drop differs between our experiments and Pathak's simulations and Meyer and Crocker's trials (see supplementary material C).

E: Estimation of the necking time

By the same method as Clanet and Lasheras[11], we estimate the characteristic necking time τ_n of a drop formed in dripping mode. We measure the neck diameter variations in time and fit our data with an exponential function in the form $D_{neck}/D_p = 1 - e^{(t-t_0)/\tau_n}$ (example given in Fig. E1), where t_0 is the moment of drop detachment.

We carry out this method for three trials on the reference system, for different (low) continuous phase velocities v_{cp}. We repeat this method for systems 1 and 2, again in dripping mode and for low v_{cp}. It should be noted that Clanet and Lasheras estimated the necking time τ_n for different nozzle diameters whereas we presently estimate τ_n for different interfacial tensions. Then, we use the same plot as Clanet and Lasheras, $1/\tau_n$ *vs* $\left(8\gamma/D_p^3\rho_{dp}\right)^{1/2}$ in Fig. E2, to determine the expression of the necking time τ_n and estimate the proportionality coefficient k' entering Eq. (8).

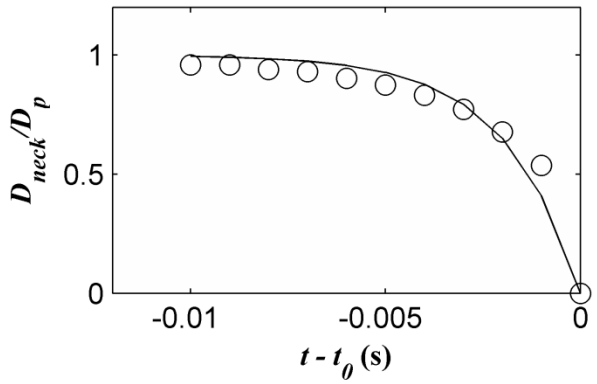

FIG. E1: Evolution of the dimensionless neck width (D_{neck}/D_p) in time: (o) reference system data, for $v_{cp} = 0.39$ m.s^{-1} and $v_{dp} = 0.031$ m.s^{-1}; exponential fit with $\tau_n = 0.0019$ s (solid line).

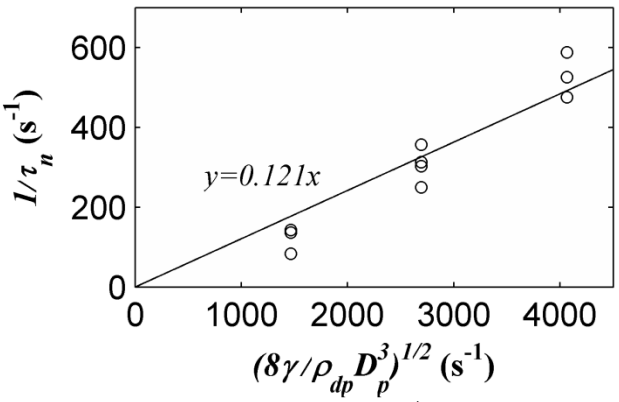

FIG. E2: Necking growth rate function of $\left(8\gamma/D_p^3\rho_{dp}\right)^{1/2}$, obtained on the reference system ($v_{cp} =$ 0.18 to 0.44 m.s^{-1}), system 1 ($v_{cp} = 0.11$ to 0.35 m.s^{-1}) and system 2 ($v_{cp} = 0.10$ to 0.20 m.s^{-1}), with $v_{dp} = 0.031$ m.s^{-1}. Fit passing through the origin (solid line).